

Enhanced Interfacial Binding and Electron Extraction Using Boron-Doped TiO₂ for Highly Efficient Hysteresis-Free Perovskite Solar Cells

Xiaoqiang Shi, Yong Ding, Shijie Zhou, Bing Zhang, Molang Cai, Jianxi Yao, Linhua Hu,* Jihuai Wu, Songyuan Dai,* and Mohammad Khaja Nazeeruddin*

Perovskite solar cells (PSCs) have witnessed astonishing improvement in power conversion efficiency (PCE), more recently, with advances in long-term stability and scalable fabrication. However, the presence of an anomalous hysteresis behavior in the current density–voltage characteristic of these devices remains a key obstacle on the road to commercialization. Herein, sol–gel-processed mesoporous boron-doped TiO₂ (B-TiO₂) is demonstrated as an improved electron transport layer (ETL) for PSCs for the reduction of hysteresis. The incorporation of boron dopant in TiO₂ ETL not only reduces the hysteresis behavior but also improves PCE of the perovskite device. The simultaneous improvements are mainly ascribed to the following two reasons. First, the substitution of under-coordinated titanium atom by boron species effectively passivates oxygen vacancy defects in the TiO₂ ETL, leading to increased electron mobility and conductivity, thereby greatly facilitating electron transport. Second, the boron dopant upshifts the conduction band edge of TiO₂, resulting in more efficient electron extraction with suppressed charge recombination. Consequently, a methylammonium lead iodide (MAPbI₃) photovoltaic device based on B-TiO₂ ETL achieves a higher efficiency of 20.51% than the 19.06% of the pure TiO₂ ETL based device, and the hysteresis is reduced from 0.13% to 0.01% with the B-TiO₂ based device showing negligible hysteresis behavior.

1. Introduction

Since the first demonstration of perovskite solar cells (PSCs) by Miyasaka and co-workers in 2009, tremendous attention has been devoted to this field due to their rapidly increased power conversion efficiency (PCE) and potentially low fabrication cost.^[1] In the past few years, the PCE of PSCs achieved an astonishing improvement from 3.8% up to 24.2%.^[2] However, one of the most critical challenges facing the PSC community is the current density–voltage (*J*–*V*) hysteresis behavior, which means that the *J*–*V* scans yield different results depending on the scan direction and scan rate.^[3] It has been considered that hysteresis is caused by the presence of both mobile ionic species and trap assisted and/or surface charge recombination.^[4] While the dominant factors affecting hysteresis are being debated within the community, one source that must be considered is the electron transport layer

Dr. X. Shi, Dr. Y. Ding, Dr. S. Zhou, Dr. B. Zhang, Dr. M. Cai,
Prof. J. Yao, Prof. S. Dai
State Key Laboratory of Alternate Electrical Power System
with Renewable Energy Sources
North China Electric Power University
Beijing 102206, P. R. China
E-mail: sydai@ncepu.edu.cn
Prof. L. Hu, Prof. S. Dai
Key Laboratory of Photovoltaic and Energy
Conservation Materials
Institute of Applied Technology
Hefei Institutes of Physical Science
Chinese Academy of Sciences
Hefei 230031, Anhui, P. R. China
E-mail: lhhu@rntek.cas.cn

Prof. J. Wu
Fujian Provincial Key Laboratory of Photoelectric
Functional Materials
Institute of Materials Physical Chemistry
Huaqiao University
Xiamen 361021, P. R. China
Prof. M. K. Nazeeruddin
Group for Molecular Engineering of Functional Materials
Institute of Chemical Sciences and Engineering
École Polytechnique Fédérale de Lausanne
CH-1951, Sion, Switzerland
E-mail: mdkhaja.nazeeruddin@epfl.ch

 The ORCID identification number(s) for the author(s) of this article can be found under <https://doi.org/10.1002/advs.201901213>.

© 2019 The Authors. Published by WILEY-VCH Verlag GmbH & Co. KGaA, Weinheim. This is an open access article under the terms of the Creative Commons Attribution License, which permits use, distribution and reproduction in any medium, provided the original work is properly cited.

DOI: 10.1002/advs.201901213

(ETL), particularly when it is composed of mesoporous titanium dioxide (TiO_2) nanoparticles.^[3b] TiO_2 is susceptible to intrinsic defects, which mainly include oxygen vacancies, cation vacancies, and cation interstitials.^[5] These nonstoichiometry defects can be ionized to form undesirable electronic defects (quasi-free electrons and electron holes) and result in reduced charge transport.^[6] As a result, PSCs based on TiO_2 with these defects suffer from strong charge accumulation and a low photovoltage. This encourages more effort to explore efficient ETLs with higher conductivity and less defects.^[7]

In order to improve the charge transport properties of TiO_2 ETLs, surface modifications and doping strategies have been developed.^[8] Tan et al. reported a contact passivation strategy using chlorine as the capping ligand to modify the low-temperature-processed TiO_2 ETL to mitigate interfacial recombination and improve the interface binding in planar PSCs. They got hysteresis-free planar PSCs with enhanced efficiency and stability.^[9] In addition, Hu et al. synthesized amino-functionalized TiO_2 nanoparticles, and achieved high efficiency with suppressed hysteresis by applying $\text{NH}_2\text{-TiO}_2$ as the ETL.^[10] Doping is another effective approach to modify both the electronic band structures and trap states of TiO_2 . To tackle this problem, a variety of dopants, such as Al, Y, Nb, and Li, have been investigated to manipulate carrier behavior.^[11] Figure S13 in the Supporting Information shows plots of the hysteresis index (HI) against dopant species for PSCs reported so far, and the detailed performance parameters are listed in Table S2 in the Supporting Information. Li dopant exhibits significant performance change in terms of reduced hysteresis, but the open-circuit voltage (V_{oc}) of PSCs is also reduced due to the downward shift of conduction band minimum (CBM) of TiO_2 .^[11d,12] It should be noted that downshift of TiO_2 CBM does not always cause V_{oc} drop as it is not the only factor affecting the voltage. V_{oc} can be enhanced or maintained when these dopants passivate electronic trap sites in the bulk and at the surface of the TiO_2 .^[11d,13] By comparison, dopants such as Nb that upshift the CBM of TiO_2 should be more desirable. Nevertheless, the hysteresis effect has not been resolved well for these dopants (Table S2 and Figure S13, Supporting Information). Doping in the TiO_2 lattice can produce considerable lattice disorder and defects, thus causing the decrease of electron mobility and the increase of parasitic recombination.^[14] Considering the theoretical model of the electrical conductivity, the ideal state is to have both high electron concentration and high electron mobility in the TiO_2 ETL simultaneously to achieve efficient electron extraction and hence balanced carrier transport. Previously, we have shown that boron (B) doping could enhance the electron injection from excited dye molecules to TiO_2 photo-anode, resulting in the increased PCE of dye-sensitized solar cells. Recently, Tian et al. reported that a low concentration of boron doping could enhance the carrier mobility and electrical conductivity of TiO_2 .^[15] Therefore, B-doped TiO_2 (abbreviated as B- TiO_2) is expected to be a desirable ETL for PSCs to synchronously improve the PCE and significantly reduce the hysteresis.

Herein, we demonstrate sol-gel-processed mesoporous B- TiO_2 as an improved ETL for PSCs. B- TiO_2 ETL exhibits upshifted CBM, increased electron mobility and conductivity, and reduced electron traps. Our density functional theory (DFT) results show that B doping leads to stronger binding

at the ETL/perovskite interface with a total binding energy of -5.41 eV for TiO_2 /perovskite interface and -6.63 eV for the B- TiO_2 /perovskite interface. These calculation results are further supported by steady-state photoluminescence (PL), time-resolved photoluminescence (TRPL), and thermal admittance spectroscopy (TAS) results. The incorporation of B dopant in TiO_2 ETL not only reduces the hysteresis behavior but also improves V_{oc} , short-circuit current density (J_{sc}), and fill factor (FF) of perovskite device. As a result, PSC based on B- TiO_2 ETL demonstrates a higher efficiency of 20.51% than 19.06% of an undoped TiO_2 ETL based device, and the hysteresis is reduced from 0.13% to 0.01% with the B- TiO_2 based device showing negligible hysteresis behavior.

2. Results and Discussion

2.1. Incorporation of Boron Dopant in TiO_2 Nanoparticles

Pure TiO_2 and B- TiO_2 nanoparticles were synthesized by a facile sol-gel method and subsequent hydrothermal treatment, as schematically illustrated in Figure S1a in the Supporting Information.^[16] In this approach, boric acid as the dopant source was added into the precursor solution to achieve a substitution doping level of 2%.^[15,16b] Transmission electron microscopy (TEM) analysis revealed that the TiO_2 and B- TiO_2 (Figure S1b,c, Supporting Information) samples are well-dispersed nanoparticles, and both have a narrow distribution in the average size of ≈ 21 nm (Figure S2, Supporting Information). The B- TiO_2 sample (Figure S1d, Supporting Information) shows an unchanged interplanar spacing of 0.358 nm for the (101) plane of anatase TiO_2 . Scanning electron microscopy (SEM) images of both TiO_2 and B- TiO_2 (Figure S1e,f, Supporting Information) films exhibit typical porous surface structure, which will facilitate the infiltration of perovskite precursor solution. Furthermore, atomic force microscopy (AFM) and corresponding cross-section SEM views show that B doping leads to a slight decrease of the root-mean-square (RMS) roughness compared to pristine TiO_2 (Figure S3, Supporting Information).

X-ray diffraction (XRD) patterns (Figure S4a, Supporting Information) confirm that a pure anatase phase (JCPDS No. 21-1272) formed after calcination and there was no observable structural difference between TiO_2 and B- TiO_2 samples. The peak positions (Figure S4b, Supporting Information) of B- TiO_2 did not show any discernible difference to pure anatase, and the values of the full width at half maximum (FWHM) of these two samples were almost the same (0.522 for TiO_2 and 0.524 for B- TiO_2). To confirm this, XRD patterns were measured of TiO_2 and B- TiO_2 powder scraped from corresponding sintered films and XRD patterns of TiO_2 and B- TiO_2 films deposited on fluorine-doped tin oxide (FTO)/cp- TiO_2 are also presented (Figure S4c,d, Supporting Information). It can be inferred that the doping level of 2% had insignificant effect on the crystal structure of TiO_2 .

To verify the form of incorporation of B in the TiO_2 lattice, X-ray photoelectron spectroscopy (XPS) measurements were conducted. Figure 1a–c compares the XPS spectra of the B 1s, Ti 2p, and O 1s peaks for doped and undoped samples, respectively. Figure 1a shows the XPS spectrum of B 1s for the B- TiO_2 sample, with a single peak centered at about 192.1 eV,

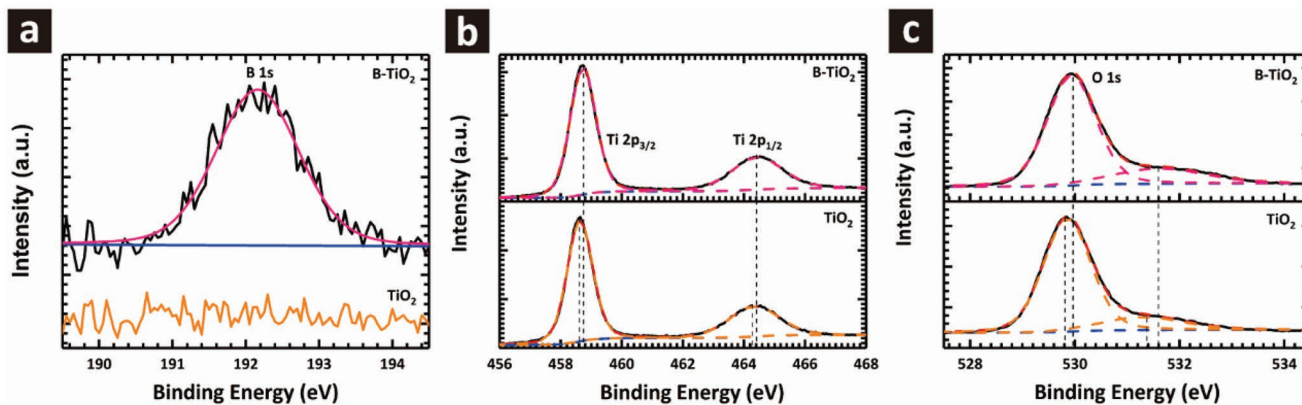


Figure 1. a) XPS spectra of B 1s peak. b) XPS spectra of Ti 2p peaks. c) XPS spectra of O 1s peaks.

which is consistent with literature values.^[17] As expected, the TiO_2 counterpart does not have a corresponding peak. Figure 1b shows the $\text{Ti} 2\text{p}_{3/2}$ and $\text{Ti} 2\text{p}_{1/2}$ peaks of the TiO_2 sample at binding energies of ≈ 464.3 and ≈ 458.6 eV, respectively, which are typical for the $\text{Ti}-\text{O}$ bonds in TiO_2 .^[18] In the case of B- TiO_2 , the $\text{Ti} 2\text{p}_{3/2}$ peak is shifted slightly higher to 458.7 eV, resulting from charge transfer through B doping, suggesting that the B dopant was incorporated in the TiO_2 lattice without the formation of a separate phase. In Figure 1c, the major component of the O 1s peaks centered at 529.9 and 530.0 eV can be ascribed to bonding with Ti and B, while the other component near the binding energies of 531.3 and 531.6 eV is generally considered to be hydrated bonds or carbonate from surface contaminations. The slightly higher O 1s binding energy for the B- TiO_2 sample further suggests the linkage of the $\text{Ti}-\text{O}-\text{B}$ bond in B- TiO_2 . Moreover, based on the XPS fitting results, the amount of B in the B- TiO_2 sample is evaluated by an elemental sensitive factor method,^[19] which reveals that the actual B doping level is 2.18 at%.

2.2. Optical and Electrical Properties of B- TiO_2 Film

High optical transmittance of the charge transport layer is crucial for maximizing the photocurrent of perovskite devices. Figure 2a compares the transmission spectra of FTO glass covered with the TiO_2 and B- TiO_2 films. Both of them display high average transmittance in the visible region, demonstrating excellent optical quality. The UV-vis absorption spectra in Figure S5 in the Supporting Information show a slight red shift with B doping. Figure 2b shows the extrapolated plots of $(Ahv)^2$ versus hv , which were obtained from the absorption spectra of TiO_2 and B- TiO_2 samples. The bandgap (denoted by E_g) of the TiO_2 is 3.81 eV while that of B- TiO_2 is 3.78 eV, which is consistent with that reported in the literature.^[20]

Ultraviolet photoelectron spectroscopy (UPS) measurements were also performed to ascertain if there is any change of the energy levels of the TiO_2 films before and after doping. Figure S6a,b in the Supporting Information shows that the secondary electron cutoffs of both TiO_2 and B- TiO_2 is 16.14 eV corresponding to the work function of ≈ 5.06 eV. Figure S6 in the Supporting Information shows valence band spectra,

from which the energy differences between the valence band (denoted by E_v) edges and Fermi level (denoted by E_f) of TiO_2 and B- TiO_2 were found to be 2.84 and 2.78 eV, respectively. The E_v of TiO_2 and B- TiO_2 was evaluated to be -7.90 and -7.84 eV, respectively. Finally, combining with optical bandgaps, the conduction band (denoted by E_c) edges of TiO_2 and B- TiO_2 were determined to be -4.09 and -4.06 eV, respectively. In Figure S6d in the Supporting Information, we illustrate that the E_c of B- TiO_2 is shifted by around 0.03 eV toward the vacuum level, which is beneficial for enhancing V_{oc} .^[14b]

In addition to energy band alignment, the carrier mobility also affects the charge transfer process. The electron mobilities of TiO_2 and B- TiO_2 samples were measured by the space charge limited current (SCLC) model employing an electron-only device configuration (Figure S7b, Supporting Information). The detailed calculation process is provided in Note S1 in the Supporting Information. Figure 2c shows current density-voltage ($J-V$) curves of the electron-only device fitting the Mott-Gurney law.^[21] The calculated electron mobility of the TiO_2 is $3.30 \times 10^{-5} \text{ cm}^2 \text{ V}^{-1} \text{ s}^{-1}$, while it increases to $1.69 \times 10^{-4} \text{ cm}^2 \text{ V}^{-1} \text{ s}^{-1}$ after B doping, about five times higher than the former. The higher electron mobility would contribute significantly to the electron transport, and therefore higher J_{sc} and FF in the perovskite cells. To determine direct current conductivity (σ_0) of TiO_2 and B- TiO_2 samples, we fabricated FTO/cp- $\text{TiO}_2/\text{TiO}_2$ or B- TiO_2/Ag devices, and the current-voltage ($I-V$) characteristics are shown in Figure 2d. The conductivity can be obtained from the slope of the $I-V$ plot, $I = \sigma_0 A D^{-1} V$, where A is the sample area (9 mm^2) and D is the film thickness (180 nm). The calculated values of the conductivity are 6.00×10^{-3} and $1.81 \times 10^{-2} \text{ mS cm}^{-1}$ for TiO_2 and B- TiO_2 , respectively, which is consistent with the variation trend of the electron mobility (Table S1, Supporting Information).

Low mobility of the ETLs indicates more trap states, which would lead to charge accumulation at the interface and poor charge transport. To investigate the effects of B doping on the electron trap state density in the TiO_2 films, the dark $I-V$ curves of TiO_2 and B- TiO_2 devices (Figure S7a, Supporting Information) were measured, as shown in Figure 2e and Figure S14 in the Supporting Information. Obviously, the linear relationship indicates an ohmic contact at low bias voltage region, while a nonlinearity increase starts to appear when the bias voltage

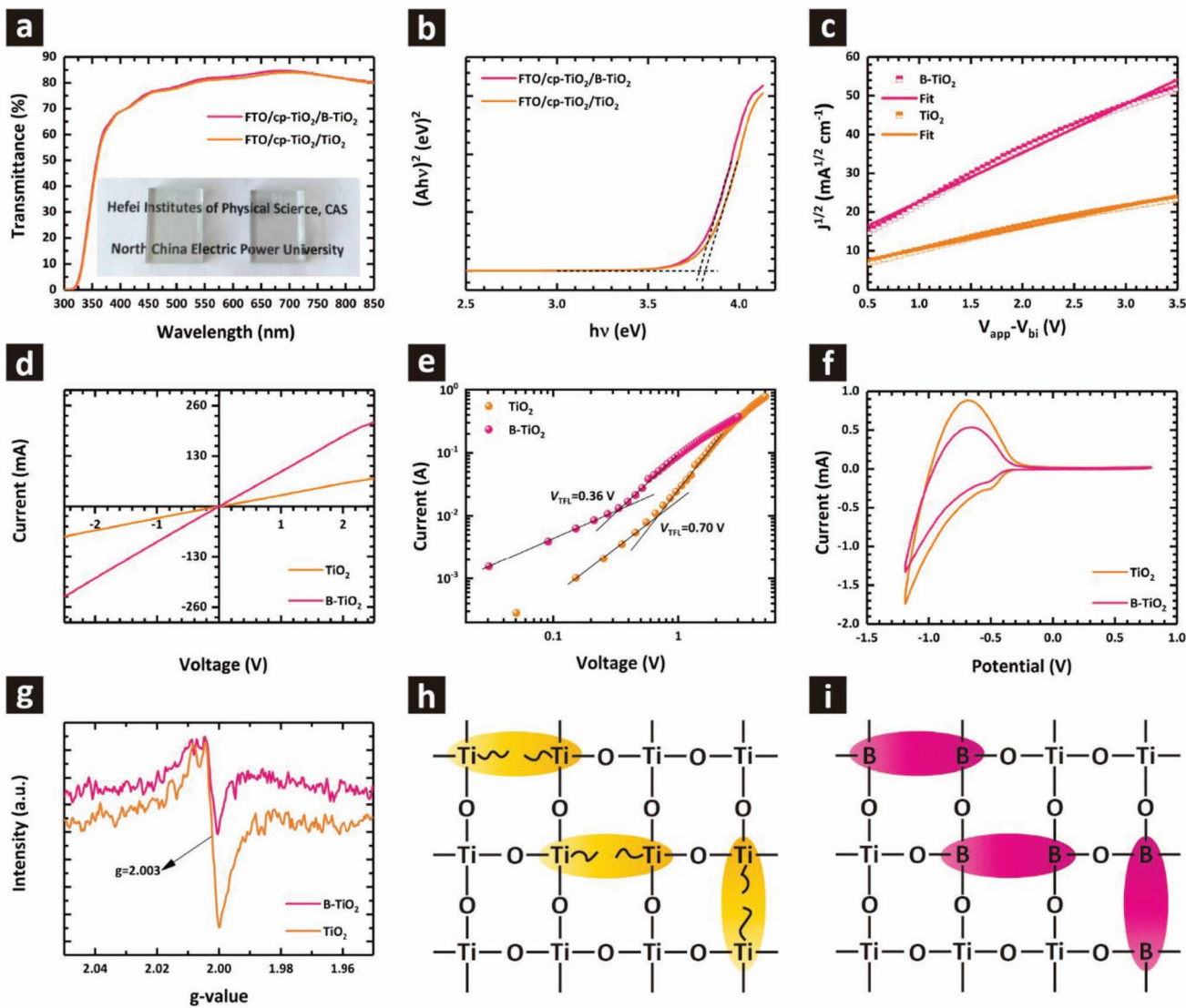


Figure 2. a) Transmittance spectra of the TiO_2 and $\text{B}-\text{TiO}_2$ films. The inset shows the corresponding photographs of both the films. b) Extrapolated plots $(\text{Ahv})^2$ versus hv obtained from the absorption spectra of TiO_2 and $\text{B}-\text{TiO}_2$ films. c) Electron mobility of TiO_2 and $\text{B}-\text{TiO}_2$ films. d) $I-V$ characteristics of the FTO/cp- $\text{TiO}_2/\text{TiO}_2/\text{Ag}$ and FTO/cp- $\text{TiO}_2/\text{B}-\text{TiO}_2/\text{Ag}$ devices. e) Log-log plot of $I-V$ curves of TiO_2 and $\text{B}-\text{TiO}_2$ devices revealing V_{TFL} tuning point behavior. f) Cyclic voltammetry of TiO_2 and $\text{B}-\text{TiO}_2$ films in LiClO_4 (0.1 M) solution. g) Electron paramagnetic resonance (EPR) spectra at 5 K for TiO_2 and $\text{B}-\text{TiO}_2$ powder. h) Oxygen vacancies in the lattice give rise to Ti defects that form deep electronic traps. i) Boron substitution in the Ti sites passivates these defects.

exceeds the inflection point, demonstrating that the trap states are completely filled. The trap-filled limit voltage (V_{TFL}) was determined by the trap state density^[22]

$$V_{\text{TFL}} = \frac{en_t L}{2\epsilon_0 \epsilon_r} \quad (1)$$

where e is the elementary charge of the electron (1.6×10^{-19} C), L is the TiO_2 film thickness (180 nm), ϵ_0 is the vacuum permittivity (8.854×10^{-12} F m $^{-1}$), ϵ_r is the relative dielectric constant of TiO_2 (55),^[23] and n_t is the trap state density. With the averaged V_{TFL} value (Figure S14, Supporting Information), the trap state density n_t in $\text{B}-\text{TiO}_2$ was calculated to be 6.39×10^{16} cm $^{-3}$. For comparison, the calculated trap state density in the TiO_2 was 1.27×10^{17} cm $^{-3}$, which is almost two times higher than

in the $\text{B}-\text{TiO}_2$. Clearly, B doping effectively passivates electron traps, resulting in the increased electron mobility.

To further understand the surface states of TiO_2 films, we conducted cyclic voltammetry (CV) analysis in LiClO_4 (0.1 M) solution. Under negative potential (forward bias), the quasi E_f of TiO_2 moved toward to E_c , leading to a capacitive current. Ideally, electron injection will commence once the quasi E_f approaches the E_c minimum. However, electrons originating from surface states level below the E_c are injected under forward bias, producing a gradual onset of the capacitive current. Under reverse bias, the capacitive current reached zero at the more positive potentials, implying recovery of the injected electrons and regeneration of most surface states. To sum up, the current peak is related to the occupancy of the surface states in the bandgap.^[24] As shown in

Figure 2f, the current peak intensity of B-TiO₂ sample decreased compared to that of TiO₂. This further confirms the reduced electron traps in the presence of B doping.

There is broad consensus that oxygen vacancies or titanium interstitials are the predominant nonstoichiometry defects in TiO₂, resulting partially from the reduction of Ti⁴⁺ to Ti³⁺ (treating the electronic structure as purely ionic while the actual electronic structure is part covalent). As a result, the inferred Ti³⁺ defects can induce a shallow energy level below the E_c and act as electron trap sites, which traps electrons and depresses electron transport and conductivity of TiO₂. Based on the above measurements and discussion, we show the trap passivation mechanism in Figure 2h,i. We speculate that the process of B doping is similar to that of Al doping, both of which involve the substitution of the inferred Ti³⁺ by a species with valency +3.^[11a] Therefore, this substitution by B effectively passivates oxygen vacancy defects in a TiO₂ ETL. This conclusion is further supported by the electron paramagnetic resonance (EPR) results as indicated in Figure 2g, in which signal originating from oxygen vacancy traps ($g = 2.003$) is significantly weakened.^[25]

2.3. Enhanced Interfacial Binding and Electron Extraction

Considering B-TiO₂ film with reduced defects, the ETL/perovskite interface can be expected to have higher binding energy, that is, be more ideal. To confirm this, we first used DFT to examine interfacial binding at the ETL/perovskite interface (Figure 3a,c). Details for DFT calculations is provided

in Note S2 in the Supporting Information. Boron doping leads to stronger binding at the ETL/perovskite interface with a total binding energy of -5.41 eV for TiO₂/perovskite interface and -6.63 eV for the B-TiO₂/perovskite interface. It indicates that B-TiO₂ film surface is more energetically favored to contact the perovskite. We speculated that the increased binding energy at B-TiO₂/perovskite interface might originate from the stronger B-I bonds.^[26] Besides, B-TiO₂/perovskite interface shows stronger Coulomb interactions as confirmed by the differential charge density across this interface.

Steady-state photoluminescence measurement was performed to study the charge transfer kinetics between perovskite and ETLs. Figure 3b comparatively shows steady-state PL spectra of methylammonium lead iodide (MAPbI₃) films where we observe a more strongly quenched PL in the B-TiO₂/perovskite stack. This result suggests that the electron extraction from the perovskite was more efficient for B-TiO₂, consistent with the high electron mobility of B-TiO₂ film and improved interfacial binding at the B-TiO₂/perovskite interface. We further investigate the modulation of charge transfer through time-resolved photoluminescence decay kinetics (Figure 3d). The TRPL decay curves were exponentially fitted with the lifetime and corresponding amplitudes listed in Table 1. Generally, the slow decay component (τ_2) can be correlated to the radiative recombination of free carriers due to bulk traps in the perovskite, and the fast decay component (τ_1) is primarily dictated by the quenching of carriers at the interface, in the present case involving the ETL/perovskite interface.^[9,12] As shown in Table 1, the time constant for fast decay component (τ_1) decreases from 8.2 to

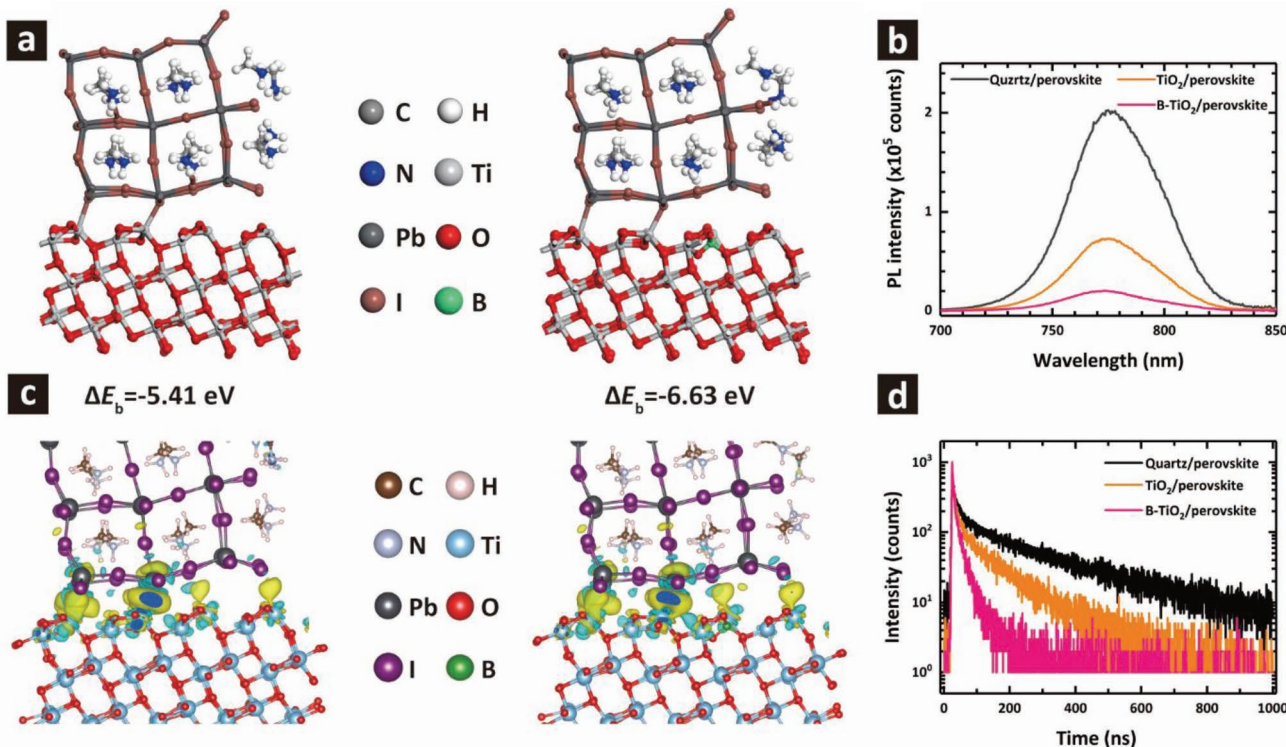


Figure 3. a,c) Binding energy and corresponding differential charge densities of the two structures. b,d) Steady-state PL spectra and TRPL decays of perovskite films on quartz and on TiO₂ and B-TiO₂ coated FTO substrates.

Table 1. TRPL decay lifetimes of perovskite films on quartz, TiO_2 , and B-TiO_2 coated FTO substrates. τ_1 and τ_2 correspond to the fast and slow decay components, respectively.

Samples	τ_1 [ns]	A_1 [%]	τ_2 [ns]	A_2 [%]	τ_{ave} [ns] ^{a)}
Quartz/perovskite	15.3	12.6	241.0	87.4	212.6
TiO_2 /perovskite	8.2	28.0	116.8	72.0	86.4
B-TiO_2 /perovskite	4.7	35.4	27.0	64.6	19.1

^{a)} $\tau_{\text{ave}} = \sum_i A_i \tau_i$, where $\sum_i A_i = 1$.

4.7 ns for perovskite cast on B-TiO_2 film, indicative of a more rapid interfacial charge transfer in the B-TiO_2 /perovskite stack. This result originates from the enhanced electron mobility and improved interface. Meanwhile, the slow decay component (τ_2) decreases from 116.8 to 27.0 ns, which may result from a reduced Shockley–Read–Hall recombination via bulk traps in the perovskite film, given the improved film quality with B-TiO_2 ETL (Figure S8, Supporting Information).^[27] Compared to the TiO_2 /perovskite sample, the calculated amplitude of τ_2 is decreased from 72.0% to 64.6%, while the calculated amplitude of τ_1 is increased from 28.0% to 35.4%, resulting in amplitude average lifetime of 86.4 and 19.1 ns for TiO_2 and B-TiO_2 based stack, respectively. Overall, these results further indicate that the interfacial binding and electron extraction are enhanced at B-TiO_2 /perovskite interface. In addition, perovskite deposited on quartz substrate shows high PL intensity and long carrier lifetime, indicating the good quality of our perovskite film.

2.4. Photovoltaic Performance of PSCs

With the superior optoelectronic properties discussed above, it is expected that the B-TiO_2 would make a better ETL in the PSCs than the TiO_2 . Mesoscopic-type PSCs were therefore fabricated based on different ETLs with the device structure shown in Figure 4a. The simple and commonly used MAPbI_3 was employed as the active absorber.

Figure 4a shows the J – V characteristics of mesoscopic-type PSCs using different ETLs, with the photovoltaic parameters, including J_{sc} , V_{oc} , FF, and PCE summarized in Table 2. The device based on TiO_2 produces a calculated PCE of 19.06% with $J_{\text{sc}} = 22.96 \text{ mA cm}^{-2}$, $V_{\text{oc}} = 1.08 \text{ V}$, and FF = 76.60%. As expected, when the B-TiO_2 is employed as ETL, the J_{sc} , V_{oc} , and FF are increased to 23.71 mA cm^{-2} , 1.10 V , and 78.60%, yielding a PCE up to 20.51%. The statistical consistency of the performance enhancement was demonstrated by comparing the performance of 24 devices (24 devices each for pure TiO_2 and B-TiO_2), and the results are shown in Figure S9 in the Supporting Information. The low device performance for the TiO_2 based PSCs is caused by relatively small J_{sc} and FF, which is related to low electron mobility and higher resistance, and the low V_{oc} results from the carrier recombination at the ETL/perovskite interface (see later discussion). By comparison, the mesoscopic-type PSCs with B-TiO_2 ETLs exhibit better performance. The higher J_{sc} and FF are attributed to the high electron mobility that promotes effective electron extraction, and the larger V_{oc} is due to the stronger bonds at the B-TiO_2 /perovskite interface that results

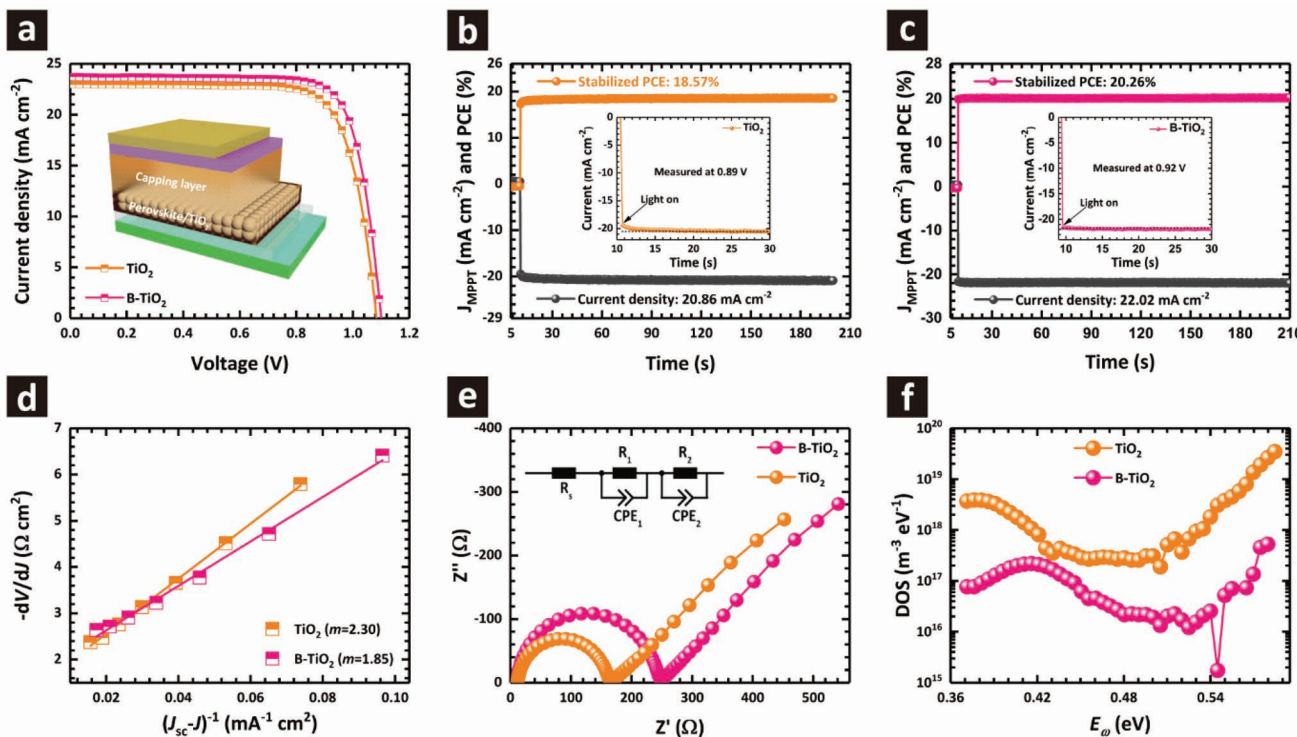


Figure 4. a) J – V curves of the devices with TiO_2 and B-TiO_2 ETLs. b,c) Steady-state power output at the maximum power point under ambient conditions (20 to 25 °C; relative humidity of 25–40%). The insets are zoomed-in view. d) Plots of $-dV/dJ$ versus $(J_{\text{sc}} - J)^{-1}$ for the typical devices and corresponding linear fitting results. e) Nyquist plots of the devices with TiO_2 and B-TiO_2 ETLs obtained at 0.8 V bias under illumination (inset shows the equivalent circuit for fitting the Nyquist plots). f) Trap density of states obtained by thermal admittance spectroscopy for devices with TiO_2 and B-TiO_2 ETLs.

Table 2. Photovoltaic parameters of MAPbI_3 solar cells based on TiO_2 and B- TiO_2 ETLs.

Devices	Scan direction	J_{sc} [mA cm^{-2}]	J_{sc} by IPCE [mA cm^{-2}]	V_{oc} [V]	FF [%]	PCE [%]	HI	Stabilized [%]
TiO_2	Reverse	22.96	21.93	1.08	76.60	19.06	0.13	18.57
	Forward	22.81		1.03	70.17	16.57		
B- TiO_2	Reverse	23.71	22.60	1.10	78.60	20.51	0.01	20.26
	Forward	23.57		1.10	78.13	20.34		

in reduced interfacial recombination. Figure S10 in the Supporting Information shows the incident photon to current conversion efficiency (IPCE) of the PSCs based on different ETLs. Integration of the IPCE spectra over the solar emission yields AM 1.5 photocurrent of 21.93 and 22.60 mA cm^{-2} for the device using TiO_2 and B- TiO_2 , respectively, which agrees well with the J_{sc} values obtained from the J - V curves within $\approx 5\%$ deviation. It can be seen that the integrated current density is lower than what is measured from the J - V curves with and without boron doping. This trend has been systematically observed also from other groups, and it can in part be attributed to a small spectral mismatch between the solar simulator and the standard AM 1.5G emission.^[28]

To further demonstrate the device characteristics, photocurrent response of the champion devices from each group based on TiO_2 and B- TiO_2 was measured when the devices were biased at 0.89 and 0.92 V, respectively. Figure 4b,c shows the corresponding curves at the maximum power point in the J - V plots. The PCEs of the champion devices using the TiO_2 and B- TiO_2 ETLs stabilize at 18.57% and 20.26% with photocurrent densities of 20.86 and 22.02 mA cm^{-2} , respectively, very close to the values measured from the J - V curves. As shown in Figure 4b,c insets, the photocurrent of the B- TiO_2 based device rose quickly to maximum steady-state photocurrent. However, photocurrent from the TiO_2 based cell needed more than 2 s to fully saturate. It indicates that it takes longer for the TiO_2 based device to reach steady state, which is consistent with the larger hysteresis of TiO_2 based devices (Table 2).^[29]

To gain further insight into the photovoltaic characteristics of TiO_2 and B- TiO_2 based devices, we analyzed the J - V characteristics based on the equivalent circuit model (Figure S12, Supporting Information). According to the equivalent circuit model, the current density J is described as^[30]

$$J = J_{\text{ph}} - J_0 \left[\exp\left(\frac{q(V + J \times R_s)}{mk_B T}\right) - 1 \right] - \frac{V + J \times R_s}{R_{\text{sh}}} \quad (2)$$

where J_{ph} is the photocurrent density, J_0 is the saturation current density at reverse bias, q is the elementary charge, m is the ideality factor, k_B is the Boltzmann's constant, T is temperature in degrees Kelvin, R_s is the series resistance, and R_{sh} is the shunt resistance. When R_s is far less than R_{sh} , Equation (2) can be expressed as

$$-\frac{dV}{dJ} = \frac{mk_B T}{q} (J_{\text{sc}} - J)^{-1} + R_s \quad (3)$$

Figure 4d displays the plots of $-\frac{dV}{dJ}$ versus $(J_{\text{sc}} - J)^{-1}$ and the linear fitting curves for TiO_2 and B- TiO_2 based devices according to Equation (3). The values of m can be derived from the linear fitting results. Compared to the TiO_2 based device,

the value of m decreased from 2.30 to 1.85. The ideality factor m depends on carrier diffusion and recombination processes.^[30a] The smaller the value of m , the less recombination is caused by traps in the device. Thus, a smaller m perhaps means that the carrier recombination in B- TiO_2 based device is reduced because of the reduction of trap states in the B- TiO_2 films.

The electrical impedance spectroscopy (EIS) measurements were conducted to extract transfer resistance in the devices. Figure 4e shows the Nyquist plots of the devices using TiO_2 and B- TiO_2 ETLs measured at 0.8 V bias under illumination, with the equivalent circuit shown in Figure 4e inset. Commonly, the high-frequency component is the signature of the transfer resistance R_{tra} (R_1) and the low-frequency component is for the recombination resistance R_{rec} (R_2).^[31] In this study, because other interfaces are identical for all devices, the only variable affecting R_{tra} is the perovskite/ETL interface. When we perform numerical fitting, the device with B- TiO_2 ETL shows smaller R_{tra} of 6.45 Ω and the larger R_{rec} of 231.4 Ω compared to that of TiO_2 based device (R_{tra} of 8.33 Ω and R_{rec} of 147.2 Ω). The smaller R_{tra} is beneficial for electron extraction, and the large R_{rec} effectively resists charge recombination, which is in agreement with the observations discussed above.

To further investigate the performance improvement by using B- TiO_2 ETL, we studied the density of trap states at the perovskite/ETL interface by performing thermal admittance spectroscopy on complete devices. By interrogating the frequency dependent capacitance via TAS measurements we can determine the energetic profile of trap density of state (DOS). As shown in Figure 4f, the B- TiO_2 based device shows more than one order of magnitude lower trap density compared to the control device, confirming that the electronic contact between perovskite and TiO_2 is enhanced through boron doping.

2.5. Hysteresis and Stability

Hysteresis and stability are two pivotal characteristics for the PSCs.^[32] For the hysteresis behavior, Figure 5a,b shows the J - V curves measured under both reverse- and forward-scan directions with the related photovoltaic parameters listed in Table 2. It is found that the device with B- TiO_2 has almost identical J - V curves with negligible hysteresis, even when it is measured using different scan rates from 1 to 500 mV s^{-1} (Figure S11, Supporting Information). To quantify the hysteresis effect, hysteric index was given by

$$\text{HI} = \frac{\text{PCE}_{\text{reverse}} - \text{PCE}_{\text{forward}}}{\text{PCE}_{\text{reverse}}} \quad (4)$$

where $\text{PCE}_{\text{reverse}}$ and $\text{PCE}_{\text{forward}}$ represent PCE for the reverse (from open-circuit to short-circuit under the forward bias

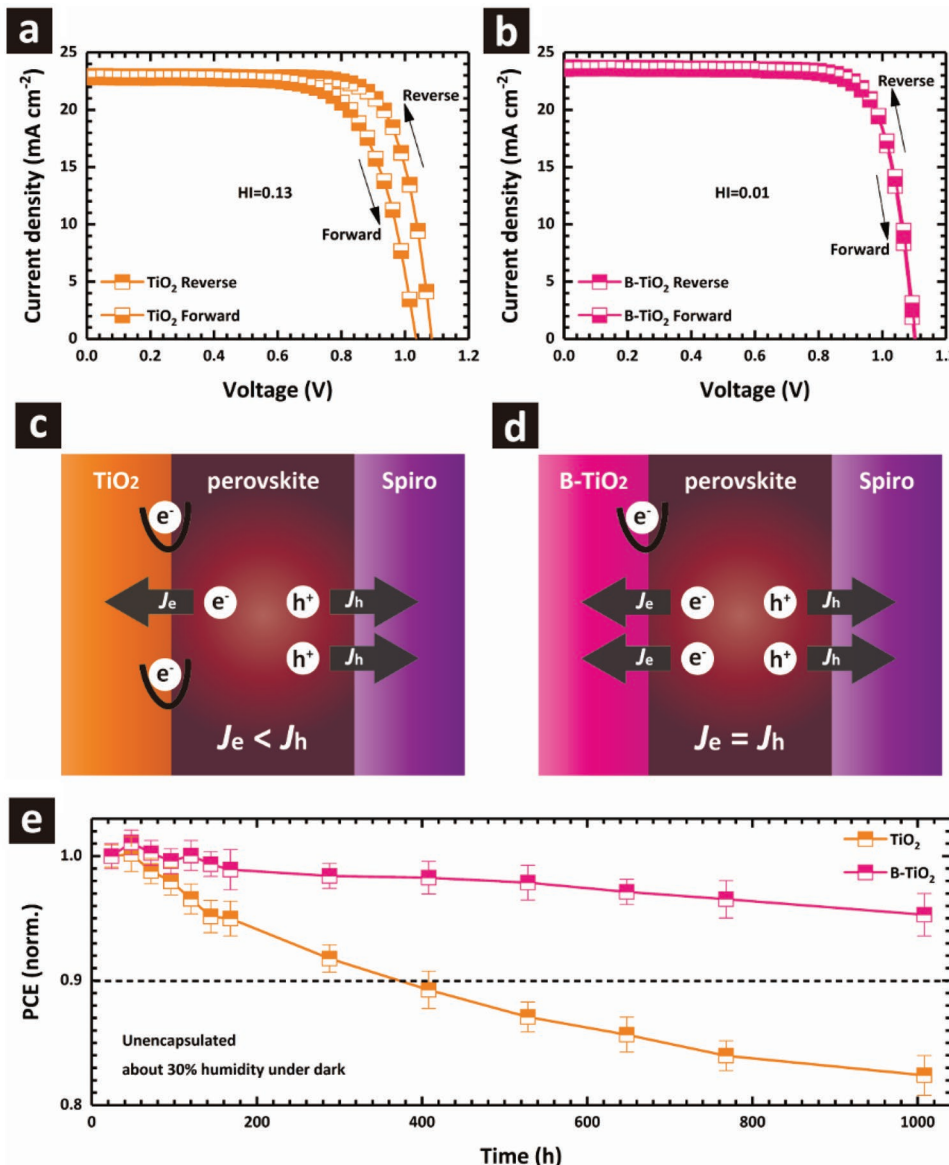


Figure 5. The J - V curves of the devices with a) TiO_2 and b) $\text{B}-\text{TiO}_2$ measured under both reverse- and forward-scan directions. Carrier transport mechanism of mesoscopic-type PSCs with c) TiO_2 and d) $\text{B}-\text{TiO}_2$ ETLs. e) Dark storage stability of unsealed MAPbI_3 cells based on TiO_2 and $\text{B}-\text{TiO}_2$ ETLs in dry air (20 to 25 °C; relative humidity of 25 – 30%). Error bars represent standard deviations of 12 individual cells for each case.

voltage) and forward (from short-circuit to open-circuit under the forward bias voltage) scans, respectively. PSCs based on $\text{B}-\text{TiO}_2$ ETL show a decreased HI of 0.01 compared to that of TiO_2 based analogue at 0.13 .

In general, the hysteresis behavior of PSCs is attributed to interfacial capacitance caused by interfacial charge accumulation, which originates from ion migration, high trap density, and unbalanced carrier transport within the device.^[4a–c,33] It is shown that the trap density at the $\text{B}-\text{TiO}_2$ /perovskite interface, one of the major causes for hysteresis, is significantly reduced. Furthermore, the electron mobility of the TiO_2 ETL is only $3.30 \times 10^{-5} \text{ cm}^2 \text{ V}^{-1} \text{ s}^{-1}$ (Figure 2c), about an order of magnitude slower than the hole mobility of the doped spiro-OMeTAD ($\approx 10^{-4} \text{ cm}^2 \text{ V}^{-1} \text{ s}^{-1}$) HTL.^[34] Therefore, the electron flux (J_e) is smaller than the hole flux (J_h), which leads to charge

accumulation at the TiO_2 /perovskite interface, as shown in Figure 5c. The accumulated carrier would give rise to hysteresis in the PSCs (Figure 5a). In combination with the high electron mobility of the $\text{B}-\text{TiO}_2$ ($1.69 \times 10^{-4} \text{ cm}^2 \text{ V}^{-1} \text{ s}^{-1}$) ETL and the larger contact area at the ETL/perovskite interface, the J_e and J_h can be balanced when the mesoscopic electron conductor ($\text{B}-\text{TiO}_2$) is employed as the ETL (Figure 5d), resulting in equivalent carrier transport at both interfaces. Thus, the high electron mobility of $\text{B}-\text{TiO}_2$ would enhance charge transport from perovskite to $\text{B}-\text{TiO}_2$ ETL, leading to reduced charge accumulation, and consequently, the devices based on the $\text{B}-\text{TiO}_2$ ETL exhibit negligible hysteresis.

Furthermore, we examined the stability of PSCs made on TiO_2 and $\text{B}-\text{TiO}_2$ ETLs under dark storage. Figure 5e shows normalized PCE measured as a function of storage time.

These PSCs had good storage stability, while the devices made on B-TiO₂ exhibited enhanced stability relative to TiO₂. The TiO₂ based device maintains 82% of the initial efficiency after dark storage in an ambient atmosphere over 1000 h, while the B-TiO₂ based analogue retains 95% of the original efficiency under the same storage condition. The stability of PSCs is closely related to the interface contact and interfacial charge recombination.^[9,11a,c] In the present work, all PSCs used the same configuration and materials except for ETLs, therefore, the degradation from other interfaces should be the same for all the PSCs. It is found that the trap states density of B-TiO₂ films is decreased and charge recombination at B-TiO₂/perovskite interface is retarded in comparison to that of pure TiO₂. The decreased trap states density of B-TiO₂ films and retarded charge recombination can facilitate the interfacial charge transfer between the perovskite and ETL so that charge accumulation and recombination within the devices can be avoided. Overall, the stronger binding at the B-TiO₂/perovskite interface and the suppressed interfacial recombination account for superior stability in mesoscopic-type PSCs based on B-TiO₂.

3. Conclusions

In summary, we have demonstrated an effective way to eliminate the hysteresis effect of PSCs resulting from the ETL by manipulating carrier transport properties using mesoporous B-TiO₂ as an improved ETL. The incorporation of B dopant in TiO₂ ETL not only reduces the hysteresis behavior but also improves V_{oc} , J_{sc} , FF, and PCE of PSCs. The simultaneous improvements are mainly ascribed to the following two reasons. First, the substitution of titanium by boron species effectively passivates oxygen vacancy defects in TiO₂ ETL, leading to increased electron mobility and conductivity, therefore greatly facilitating electron transport. Meanwhile, our DFT calculations also show that B doping leads to stronger binding at the ETL/perovskite interface with a total binding energy of -5.41 eV for TiO₂/perovskite interface and -6.63 eV for B-TiO₂/perovskite interface, due to diminished trap states. This enhanced interfacial binding ensures superior electronic contact between the perovskite and ETL. Second, B dopant upshifts the conduction band edge of TiO₂, resulting in more efficient electron extraction with suppressed charge recombination. As a result, PSCs based on B-TiO₂ ETL demonstrate a higher efficiency of 20.51% than 19.06% of the device with pure TiO₂ ETL, and the hysteresis is reduced from 0.13% to 0.01% with the B-TiO₂ based device showing negligible hysteresis behavior.

4. Experimental Section

Preparation of TiO₂ Materials: 60 mL of titanium (IV) isopropoxide (TTIP) (Sigma-Aldrich, 97%) was added dropwise to a solution consisting of 140 mL of deionized water and 60 mL of ethanol in a 500 mL beaker under vigorous stirring, and the formed precipitate solution was stirred intensely for 4 h after the drip process was finished. After that, the mixture was filtered with a 250 mL G5 sand core funnel, and the precipitate was washed three times with deionized water during the filtration process. The precipitate was then transferred to a Teflon round container (inside volume, 450 mL) containing 90 g trimethylamine

aqueous solution (6.58 wt%), and the solution was stirred for 14 h at a temperature of 80–85 °C to form a translucent sol, after which another 10 g of trimethylamine aqueous solution was added and further stirred for 10 min at room temperature. Subsequently, the resulting sol was transferred into Teflon containers (inside volume, 100 mL) and placed in sealed metal autoclave vessels, which were then placed in an oven for 10 h at 200 °C. The obtained gel was diluted with ethanol and was evaporated on a rotary evaporator to remove most of the water, and the gel was then purified by rinsing with ethanol three times and centrifuged. For the doped samples, 8.04 g boric acid (Sigma-Aldrich, 99.5%) was dissolved in a mixed solution of deionized water and ethanol, and stirred for 30 min before the addition of TTIP. TiO₂ pastes were then prepared according to previously reported procedures.^[16a]

Fabrication of Perovskite Devices: All devices were prepared in ambient air. The TiO₂ compact (cp-TiO₂) layer was prepared by a spray pyrolysis method: a solution containing 0.4 mL of acetylacetone and 0.6 mL of TTIP in 7 mL of isopropanol was sprayed on cleaned and patterned FTO (Pilkington, 15 Ω sq⁻¹) substrates at 460 °C using dry air as a carrier gas. Then, the mesoporous TiO₂ (mp-TiO₂) and B-doped TiO₂ films were spin-coated onto the FTO/cp-TiO₂ substrate using as-prepared pastes and calcined at 510 °C for 30 min in air to remove organic components. The perovskite layer was deposited from a precursor solution containing 1.2 M PbI₂ (Alfa, 99.999%) and 1.2 × 0.98 M CH₃NH₃I (Dyesol, 99.9%) in a mixed solvent of DMF and DMSO, in which the volume ratio of DMF to DMSO was 1:4. The perovskite precursor solution was spin-coated on FTO/cp-TiO₂/mp-TiO₂ substrate by a consecutive two-step spin-coating program at 1100 and 4200 rpm for 15 and 30 s, respectively. During the second step, 110 μL of chlorobenzene was poured onto the spinning substrate 10 s prior the end of the program. The films were then annealed on a hotplate at 100 °C for 15 min. Once cooled down to room temperature, Spiro-OMeTAD (Xi'an Polymer Light Technology Corp.) was deposited on top of the perovskite layer by spin coating at 4500 rpm for 20 s. The Spiro-OMeTAD solution was prepared by dissolving 73.53 mg of Spiro-OMeTAD in 1 mL chlorobenzene, with the addition of 29.30 μL of 4-tert-butylpyridine (tBP, Sigma-Aldrich, 96%), 17.22 μL of lithium bis(trifluoromethanesulfonyl)imide (Li-TFSI, Sigma-Aldrich, 99.8%) solution (500 mg Li-TFSI in 1 mL acetonitrile), and 6.78 μL of tris(2-(1H-pyrazol-1-yl)-4-tert-butylpyridine)-cobalt(III) tris(bis(trifluoromethylsulfonyl)imide) (FK209, Dyenamo AB) solution (400 mg FK209 in 1 mL acetonitrile).^[35] Finally, an 80 nm gold layer was thermally evaporated on top of the device.

Characterization: The morphology measurement was taken by SEM (SU8010, Hitachi, Japan) and TEM (Tecnai G2 F30, FEI, USA). The composition and crystal structure were analyzed by XRD (D8 FOCUS, Bruker, Germany). XPS and UPS measurements were performed on the ESCALAB 250Xi (Thermo Scientific) with different radiation source. The film roughness was collected on an atomic force microscope (5500, Keysight, USA). The contact angle measurement was carried out by a contact angle meter (JC200D3, Powereach, China). The UV-vis absorption spectra were recorded with a spectrophotometer (UV-3600Plus, Shimadzu, Japan). Steady PL was obtained from a fluorescence spectrometer (FLS980, Edinburgh, UK) with the pump light wavelength of 485 nm and the probe light wavelength of 770 nm.

J-V curves were recorded by using a Keithley 2420 source meter under simulated sunlight from Newport solar simulator matching the AM 1.5G standard with an intensity of 100 mW cm⁻². A nonreflective metal mask with an aperture area of 0.09 cm² was used to define the active area of the device. The IPCE curves were confirmed as a function of wavelength from 300 to 800 nm (PV Measurements, Inc.). The IS measurement was carried out on an electrochemical workstation (Zennium pro, Zahner, Germany) in the frequency range of 10 mHz to 1 MHz under AM 1.5G condition.

Supporting Information

Supporting Information is available from the Wiley Online Library or from the author.

Acknowledgements

This work was supported by the National Key Research and Development Program of China (No. 2016YFA0202400), the 111 Project (No. B16016), the National Natural Science Foundation of China (Nos. 51702096 and U1705256), the Major/Innovative Program of Development Foundation of Hefei Center for Physical Science and Technology (2016FXZY003), the Fundamental Research Funds for the Central Universities (2018QN063), Beijing Key Laboratory of Novel Thin-Film Solar Cells, and Beijing Key Laboratory of Energy Safety and Clean Utilization. The authors thank Dr. Wei Nong from Sun Yat-sen University for the helpful discussions.

Conflict of Interest

The authors declare no conflict of interest.

Keywords

charge transport, hysteresis, interfacial binding, perovskite solar cells, titanium dioxide

Received: May 21, 2019

Revised: July 28, 2019

Published online:

- [1] a) A. Kojima, K. Teshima, Y. Shirai, T. Miyasaka, *J. Am. Chem. Soc.* **2009**, *131*, 6050; b) M. Cai, Y. Wu, H. Chen, X. Yang, Y. Qiang, L. Han, *Adv. Sci.* **2017**, *4*, 1600269; c) S. Ma, M. Cai, T. Cheng, X. Ding, X. Shi, A. Alsaedi, T. Hayat, Y. Ding, Z. Tan, S. Dai, *Sci. China Mater.* **2018**, *61*, 1257.
- [2] NREL, Best Research-Cell Efficiencies, <https://www.nrel.gov/pv/assets/pdfs/best-research-cell-efficiencies-190416.pdf> (accessed: May 2019).
- [3] a) S. N. Haberreutinger, N. K. Noel, H. J. Snaith, *ACS Energy Lett.* **2018**, *3*, 2472; b) S. Ravishankar, S. Gharibzadeh, C. Roldán-Carmona, G. Grancini, Y. Lee, M. Ralaiarisoa, A. M. Asiri, N. Koch, J. Bisquert, M. K. Nazeeruddin, *Joule* **2018**, *2*, 788; c) Y. Zhu, K. Deng, H. Sun, B. Gu, H. Lu, F. Cao, J. Xiong, L. Li, *Adv. Sci.* **2018**, *5*, 1700614.
- [4] a) C. Eames, J. M. Frost, P. R. F. Barnes, B. C. O'Regan, A. Walsh, M. S. Islam, *Nat. Commun.* **2015**, *6*, 7497; b) S. van Reenen, M. Kemerink, H. J. Snaith, *J. Phys. Chem. Lett.* **2015**, *6*, 3808; c) P. Lopez-Varo, J. A. Jiménez-Tejada, M. García-Rosell, J. A. Anta, S. Ravishankar, A. Bou, J. Bisquert, *ACS Energy Lett.* **2017**, *2*, 1450; d) I. Ka, I. M. Asuo, S. Basu, P. Fourmont, D. M. Gedamu, A. Pignolet, S. G. Cloutier, R. Nechache, *Small* **2018**, *14*, 1802319.
- [5] a) M. K. Nowotny, L. R. Sheppard, T. Bak, J. Nowotny, *J. Phys. Chem. C* **2008**, *112*, 5275; b) J. Nowotny, M. A. Alim, T. Bak, M. A. Idris, M. Ionescu, K. Prince, M. Z. Sahdan, K. Sopian, M. A. Mat Teridi, W. Sigmund, *Chem. Soc. Rev.* **2015**, *44*, 8424.
- [6] a) Y. Du, H. Cai, Y. Wu, Z. Xing, Z. Li, J. Xu, L. Huang, J. Ni, J. Li, J. Zhang, *Phys. Chem. Chem. Phys.* **2017**, *19*, 13679; b) Y.-C. Ho, M. N. F. Hoque, E. Stoneham, J. Warzywoda, T. Dallas, Z. Fan, *J. Phys. Chem. C* **2017**, *121*, 23939.
- [7] X. Shi, R. Chen, T. Jiang, S. Ma, X. Liu, Y. Ding, M. Cai, J. Wu, S. Dai, *Sol. RRL* **2019**, 1900198.
- [8] C. Zhen, T. Wu, R. Chen, L. Wang, G. Liu, H.-M. Cheng, *ACS Sustainable Chem. Eng.* **2019**, *7*, 4586.
- [9] H. Tan, A. Jain, O. Voznyy, X. Lan, F. P. García de Arquer, J. Z. Fan, R. Quintero-Bermudez, M. Yuan, B. Zhang, Y. Zhao, F. Fan, P. Li, L. N. Quan, Y. Zhao, Z.-H. Lu, Z. Yang, S. Hoogland, E. H. Sargent, *Science* **2017**, *355*, 722.
- [10] W. Hu, W. Zhou, X. Lei, P. Zhou, M. Zhang, T. Chen, H. Zeng, J. Zhu, S. Dai, S. Yang, S. Yang, *Adv. Mater.* **2019**, *31*, 1806095.
- [11] a) S. K. Pathak, A. Abate, P. Ruckdeschel, B. Roose, K. C. Gödel, Y. Vaynzof, A. Santhala, S.-I. Watanabe, D. J. Hollman, N. Noel, A. Sepe, U. Wiesner, R. Friend, H. J. Snaith, U. Steiner, *Adv. Funct. Mater.* **2014**, *24*, 6046; b) H. Zhou, Q. Chen, G. Li, S. Luo, T.-b. Song, H.-S. Duan, Z. Hong, J. You, Y. Liu, Y. Yang, *Science* **2014**, *345*, 542; c) W. Chen, Y. Wu, Y. Yue, J. Liu, W. Zhang, X. Yang, H. Chen, E. Bi, I. Ashraful, M. Grätzel, L. Han, *Science* **2015**, *350*, 944; d) F. Giordano, A. Abate, J. P. Correa Baena, M. Saliba, T. Matsui, S. H. Im, S. M. Zakeeruddin, M. K. Nazeeruddin, A. Hagfeldt, M. Grätzel, *Nat. Commun.* **2016**, *7*, 10379.
- [12] J. H. Heo, M. S. You, M. H. Chang, W. Yin, T. K. Ahn, S.-J. Lee, S.-J. Sung, D. H. Kim, S. H. Im, *Nano Energy* **2015**, *15*, 530.
- [13] I. Jeong, H. Jung, M. Park, J. S. Park, H. J. Son, J. Joo, J. Lee, M. J. Ko, *Nano Energy* **2016**, *28*, 380.
- [14] a) X. Lü, X. Mou, J. Wu, D. Zhang, L. Zhang, F. Huang, F. Xu, S. Huang, *Adv. Funct. Mater.* **2010**, *20*, 509; b) B. Roose, S. Pathak, U. Steiner, *Chem. Soc. Rev.* **2015**, *44*, 8326.
- [15] H. Tian, F. Xin, X. Tan, W. Han, J. Mater. Chem. A **2014**, *2*, 10599.
- [16] a) L. Hu, S. Dai, J. Weng, S. Xiao, Y. Sui, Y. Huang, S. Chen, F. Kong, X. Pan, L. Liang, K. Wang, *J. Phys. Chem. B* **2007**, *111*, 358; b) H. Tian, L. Hu, C. Zhang, S. Chen, J. Sheng, L. Mo, W. Liu, S. Dai, *J. Mater. Chem.* **2011**, *21*, 863.
- [17] a) W. Zhao, W. Ma, C. Chen, J. Zhao, Z. Shuai, *J. Am. Chem. Soc.* **2004**, *126*, 4782; b) N. Lu, X. Quan, J. Li, S. Chen, H. Yu, G. Chen, *J. Phys. Chem. C* **2007**, *111*, 11836.
- [18] a) C. D. Wagner, *Handbook of X-Ray Photoelectron Spectroscopy*, Perkin-Elmer, Eden Prairie, MN **1979**; b) Z.-Z. Yang, H.-Y. Wang, L. Lu, C. Wang, X.-B. Zhong, J.-G. Wang, Q.-C. Jiang, *Sci. Rep.* **2016**, *6*, 22990.
- [19] X. Meng, L. Tang, J. Li, *J. Phys. Chem. C* **2010**, *114*, 17569.
- [20] a) M.-C. Wu, S.-H. Chan, K.-M. Lee, S.-H. Chen, M.-H. Jao, Y.-F. Chen, W.-F. Su, *J. Mater. Chem. A* **2018**, *6*, 16920; b) P. Malliga, J. Pandiarajan, N. Prithivikumaran, K. Neyvasagam, *J. Appl. Phys.* **2014**, *6*, 22.
- [21] A. M. Goodman, A. Rose, *J. Appl. Phys.* **1971**, *42*, 2823.
- [22] R. H. Bube, *J. Appl. Phys.* **1962**, *33*, 1733.
- [23] L. Kavan, N. Tétreault, T. Moehl, M. Grätzel, *J. Phys. Chem. C* **2014**, *118*, 16408.
- [24] a) Z. Zhang, S. M. Zakeeruddin, B. C. O'Regan, R. Humphry-Baker, M. Grätzel, *J. Phys. Chem. B* **2005**, *109*, 21818; b) J. Zheng, L. Mo, W. Chen, L. Jiang, Y. Ding, Z. Li, L. Hu, S. Dai, *Nano Res.* **2017**, *10*, 3671.
- [25] L. Y. Ozer, H. Apostoleris, F. Ravaux, S. I. Shylin, F. Mamedov, A. Lindblad, F. O. L. Johansson, M. Chiesa, J. Sá, G. Palmisano, *ChemCatChem* **2018**, *10*, 2949.
- [26] W. Xiao, W. H. Pu, J. W. Wang, X. Wang, L. Sun, J. D. Cui, L. G. Wang, *Appl. Surf. Sci.* **2019**, *492*, 369.
- [27] J. Chen, N.-G. Park, *Adv. Mater.* **2018**, 1803019.
- [28] J.-Y. Seo, T. Matsui, J. Luo, J.-P. Correa-Baena, F. Giordano, M. Saliba, K. Schenk, A. Ummadisingu, K. Domanski, M. Hadadian, A. Hagfeldt, S. M. Zakeeruddin, U. Steiner, M. Grätzel, A. Abate, *Adv. Energy Mater.* **2016**, *6*, 1600767.
- [29] K.-H. Jung, J.-Y. Seo, S. Lee, H. Shin, N.-G. Park, *J. Mater. Chem. A* **2017**, *5*, 24790.
- [30] a) J. Shi, J. Dong, S. Lv, Y. Xu, L. Zhu, J. Xiao, X. Xu, H. Wu, D. Li, Y. Luo, Q. Meng, *Appl. Phys. Lett.* **2014**, *104*, 063901; b) J. Chen, J. Xu, L. Xiao, B. Zhang, S. Dai, J. Yao, *ACS Appl. Mater. Interfaces* **2017**, *9*, 2449.

- [31] Y.-K. Ren, X.-H. Ding, Y.-H. Wu, J. Zhu, T. Hayat, A. Alsaedi, Y.-F. Xu, Z.-Q. Li, S.-F. Yang, S.-Y. Dai, *J. Mater. Chem. A* **2017**, *5*, 20327.
- [32] a) X. Ding, Y. Ren, Y. Wu, Y. Xu, J. Zhu, T. Hayat, A. Alsaedi, Z. Li, Y. Huang, S. Dai, *Sci. China Mater.* **2018**, *61*, 73; b) Q. Fu, X. Tang, B. Huang, T. Hu, L. Tan, L. Chen, Y. Chen, *Adv. Sci.* **2018**, *5*, 1700387; c) C. Liu, X. Zhou, S. Chen, X. Zhao, S. Dai, B. Xu, *Adv. Sci.* **2019**, *6*, 1801169.
- [33] B. Chen, M. Yang, X. Zheng, C. Wu, W. Li, Y. Yan, J. Bisquert, G. Garcia-Belmonte, K. Zhu, S. Priya, *J. Phys. Chem. Lett.* **2015**, *6*, 4693.
- [34] X. Gu, Y. Li, Y. Mu, M. Zhang, T. Lu, P. Wang, *RSC Adv.* **2018**, *8*, 9409.
- [35] D. Bi, W. Tress, M. I. Dar, P. Gao, J. Luo, C. Renevier, K. Schenk, A. Abate, F. Giordano, J.-P. Correa Baena, J.-D. Decoppet, S. M. Zakeeruddin, M. K. Nazeeruddin, M. Grätzel, A. Hagfeldt, *Sci. Adv.* **2016**, *2*, e1501170.